RSC Advances

PAPER

View Article Online
View Journal | View Issue

Check for updates

Cite this: *RSC Adv.*, 2022, **12**, 8394

Initiating a high-temperature zinc ion battery through a triazolium-based ionic liquid†

Xun Li,[a] Fawen Ning,[b] Lin Luo,[b] Jianhua Wu,*[a] Yanhong Xiang,[a] Xianwen Wu,[b] Lizhi Xiong[c] and Xiaochun Peng*[b]

Triazolium-based ionic liquids (**T1**, **T2** and **T3**) with or without terminal hydroxyl groups were prepared *via* Cu(I) catalysed azide–alkyne click chemistry and their properties were investigated using various technologies. The hydroxyl groups obviously affected their physicochemical properties, where with a decrease in the number of hydroxyl groups, their stability and conductivity were enhanced. **T1**, **T2** and **T3** showed relatively high thermal stability, and their electrochemical stability windows (ESWs) were 4.76, 4.11 and 3.52 V, respectively. **T1S-20** was obtained *via* the addition of zinc trifluoromethanesulfonic acid ($Zn(CF_3SO_3)_2$) and lithium bis(trifluoromethanesulfonyl)imide (LiTFSI) to **T1**, displaying conductivity and ESW values of 1.55×10^{-3} S cm^{-1} and 6.36 V at 30 °C, respectively. Subsequently, a Zn/$Li_3V_2(PO_4)_3$ battery was assembled using **T1S-20** as the electrolyte and its performances at 30 °C and 80 °C were investigated. The battery showed a capacity of 81 mA h g^{-1} at 30 °C, and its capacity retention rate was 89% after 50 cycles. After increasing the temperature to 80 °C, its initial capacity increased to 111 mA h g^{-1} with a capacity retention rate of 93.6% after 100 cycles, which was much higher than that of the aqueous electrolyte (**WS-20**)-based zinc ion battery (71.8%). Simultaneously, the **T1S-20** electrolyte-based battery exhibited a good charge/discharge efficiency, and its Coulomb efficiency was 99%. Consequently, the **T1S-20** electrolyte displayed a better performance in the Zn/$Li_3V_2(PO_4)_3$ battery than that with the aqueous electrolyte, especially at high temperature.

Received 15th January 2022
Accepted 2nd March 2022

DOI: 10.1039/d2ra00298a

rsc.li/rsc-advances

Open Access Article. Published on 16 March 2022. Downloaded on 2/7/2026 3:14:08 PM.
This article is licensed under a Creative Commons Attribution-NonCommercial 3.0 Unported Licence.

Introduction

Zinc ion batteries (ZIBs) have been widely investigated due to their high theoretical capacity, cyclic stability, energy density and rate performance.[1–3] Besides, they can be easily assembled in air and are safer and more environmentally friendly than lithium-ion batteries, especially with the emergence of aqueous ZIBs.[4,5] However, water-induced side reactions hinder their further development, such as hydrogen/oxygen evolution reactions, dissolution of cathode materials, and narrow electrochemical stability window (ESW). In addition, the growth of dendrites needs to be suppressed.[6,7] Although high-performance cathodes have been developed to overcome the above-mentioned problems,[8–10] the electrolyte also directly affects the performance of ZIBs.[11] Concentrated salt and other additives (organic solvents and ionic liquids)[12–15] were incorporated in aqueous electrolytes by tuning the solvation sheath of Zn^{2+} to promote the plating/stripping and migration of Zn^{2+}.[16] However, the water-induced side reactions are inevitable, and thus the development of new electrolytes without water, such as organic electrolytes and solid (or quasi-solid) electrolytes, is very important.[17]

Ionic liquids (ILs), which are obtained *via* the quaternization of molecules containing nitrogen, phosphorus, sulfur atoms, *etc.*, possess the properties of low vapor pressure, appropriate conductivity, wide ESW and non-flammable nature, and hence can be considered safer than conventional organic electrolytes and better electrode interfacial contacts than solid electrolytes. However, the relatively poor stability of common ILs at high temperature limits their application.[18] Among them, imidazolium ILs are the most widely investigated,[19] where an improvement in their stability is usually realized *via* C-2 substitution but their functionalization is relative tedious.[20] Triazolium ILs possess similar chemical structures to that of imidazolium ILs but show higher stability and wider ESW,[20–22] and the emergence of azide–alkyne click chemistry allows the convenient and flexible functionalization of triazolium. To date, triazolium ILs have been studied as conductive units in polyelectrolytes,[23,24] but seldomly reported as IL electrolytes for electrochemical energy storage devices. As is known, the main shortcoming of ILs is their high viscosity, which limits their conductivity and hinders the diffusion of ions, and thus some strategies have

[a]*College of Physics and Electromechanical Engineering, Jishou University, Jishou, 416000, China. E-mail: jianhuawu@jsu.edu.cn*

[b]*College of Chemistry and Chemical Engineering, Jishou University, Jishou, 416000, China. E-mail: pnfxz@jsu.edu.cn*

[c]*College of Pharmacy, Jishou University, Jishou, 416000, China*

† Electronic supplementary information (ESI) available: ^{1}H NMR and ^{13}C NMR spectra of ILs **T1**, **T2**, **T3** and corresponding intermediates, Nyquist plots of and conductivities of ILs. See DOI: 10.1039/d2ra00298a

© 2022 The Author(s). Published by the Royal Society of Chemistry

Open Access Article. Published on 16 March 2022. Downloaded on 2/7/2026 3:14:08 PM.
This article is licensed under a Creative Commons Attribution-NonCommercial 3.0 Unported Licence.

been developed to overcome this, such as the addition of water or conventional organic electrolytes. Increasing the temperature provides another effective strategy for improving the conductivity and accelerating the migration of ions. Meanwhile, high-temperature ZIBs have rarely been reported, with the focus on conductive iongel or organohydrogel electrolyte.[25–27] In this contribution, triazolium-based ILs, **1**, **2**, and **3**, with different amounts of hydroxyl groups were synthesized *via* Cu(I)-catalysed azide–alkyne click chemistry, where we anticipated that the presence of oxygen atoms could enhance the flexibility of their side chain due to the fact that the ether group possesses a higher degree of conformational freedom than alkyl chains.[28] This is beneficial for dissolving metal ions and improving the conductivity,[29] similar to alkali-metal salt dissolved in polyether, and the influence of their molecular structure on their properties were investigated to evaluate their application in ZIBs, especially at high temperature.

Experimental

Materials

Triethylene glycol monomethyl ether, propargyl bromide, NaH (60%), iodomethane (CH_3I), triethylene glycol, L-ascorbic acid (Vc) and $CuSO_4 \cdot 5H_2O$ were purchased from Shanghai Adamas Reagent Company. Lithium bis(trifluoromethanesulfonyl)imide (LiTFSI) and zinc trifluoromethanesulfonate ($Zn(CF_3SO_3)_2$) were purchased from Shanghai Energy Chemical Co., LTD. $Li_3V_2(PO_4)_3$, compound **5**, and compound **8** were prepared according to the literature.[30–32]

Characterization

NMR spectra were recorded on a Bruker DPX500 spectrometer using tetramethyl silane as an internal standard in $CDCl_3$ or DMSO-d_6. Thermal gravimetric analysis (TGA) was performed using a Mettler-Toledo TGA 2 instrument under an argon flow at a heating rate of 10 °C min^{-1} from 30 °C to 800 °C. Differential scanning calorimetry (DSC) was performed on a Netzsch 204F1 in a nitrogen atmosphere. An indium standard was used for the temperature and enthalpy calibrations. The sample was first heated from 25 °C to 150 °C and held at this temperature for 3 min to eliminate the thermal history, and then cooled to −90 °C and heated again from −90 °C to 100 °C, at a heating or cooling rate of 10 °C min^{-1}. Conductivity was measured according to our previous method[33] *via* electrochemical impedance spectroscopy (EIS) on a CHI 760E electrochemical workstation (Shanghai Chenhua Equipment, China) with an AC amplitude of 10 mV in the frequency range of 0.01 Hz to 100 kHz, and the conductivity 'σ' was calculated using the formula $\sigma = D/(SR)$, where 'D' is the thickness of the sample and 'S' is the area of the sample.

The assembly of CR2016-type coin cells was as follows: a slurry consisting of $Li_3V_2(PO_4)_3$ (70 wt%), acetylene black (20 wt%), polyvinylidene fluoride (10 wt%), and *N*-methylpyrrolidone was pasted on stainless steel mesh, then dried at 80 °C for 12 h, and finally cut into round pieces as cathodes. The mass loading of $Li_3V_2(PO_4)_3$ was approximately 2 mg per piece. CR2016-type coin cells were assembled in an open atmosphere by sandwiching a Whatman filter paper soaked with electrolyte between the prepared $Li_3V_2(PO_4)_3$ cathode and zinc foil anode.

The ESWs of the ILs were measured on a CHI760E electrochemical workstation *via* linear sweep voltammetry (LSV) at a scanning rate of 1 mV s^{-1} in different voltage ranges by sandwiching the electrolyte between a stainless steel sheet cathode and zinc foil anode. Cyclic voltammetry (CV) measurement of the CR2016-type coin cells was carried out on a CHI760E electrochemical workstation at a scanning rate of 0.1 mV s^{-1}. The charge/discharge performance of the CR2016-type coin cells was tested on a Neware battery test system (Shenzhen Neware Electronics Co., Ltd). The cycle stability of the ZIBs at the rate of 0.2 A g^{-1} and their rate performance at different current densities (0.2, 0.3, 0.5, 1, and 1.5 A g^{-1}) were tested in the voltage range of 0.7–1.7 V. Scanning electron microscopy (SEM, TESCAN MIRA4) was used to observe the morphological characteristics of the Zn foil anode.

Synthetic procedures

Synthesis of compound 1. To a 500 mL dry three-neck bottle flask, anhydrous THF (100 mL) and NaH (6 g, 150 mmol) were added under nitrogen at 0 °C, and then triethylene glycol monomethyl ether (16.4 g, 100 mmol) in anhydrous THF (50 mL) was added dropwise. After stirring for 1 h, the mixture was placed in ice bath and propargyl bromide (14.2 g, 120 mmol) in anhydrous THF (50 mL) was added slowly, and then warmed to room temperature and stirred for 24 h. Subsequently, the mixture was dropped into 100 mL of ice water and extracted with ethyl acetate, then washed with saturated brine, and the organic phase was dried over anhydrous $MgSO_4$ and filtered. After removal of the solvent, the crude product was purified *via* column chromatography (petroleum ether: ethyl acetate = 4 : 1) to yield compound **1** as a light-yellow oil (18 g, yield 89.11%).

Synthesis of compound 2. To a 500 mL dry three-neck bottle flask, triethylene glycol monomethyl ether (24.6 g, 150 mmol) and triethylamine (34.6 mL, 250 mmol) were added at 0 °C, and then *p*-toluene sulfonyl chloride (23.9 g, 125 mmol) dissolved in dichloromethane (50 mL) was added dropwise and warmed to room temperature. After stirring for 24 h, the mixture was adjusted to acidic with dilute hydrochloric acid, and then washed with deionized water, saturated brine, and extracted with dichloromethane. The organic phase was dried over anhydrous $MgSO_4$. After removal of the solvent, the crude product was obtained (37 g) and used without further purification.

The crude product (37 g), acetonitrile (100 mL) and NaN_3 (6.11 g, 116 mmol) were added to a 500 mL flask and stirred at 90 °C for 7 d. The reaction solution was filtered and concentrated, and then diluted with ethyl acetate (200 mL) and washed with saturated brine. The organic phase was collected and dried over anhydrous $MgSO_4$. After removal of the solvent, the crude product was purified *via* column chromatography (petroleum ether: ethyl acetate = 4 : 1) to yield compound **2** as a light-yellow oil (15.2 g, 70% yield).

Open Access Article. Published on 16 March 2022. Downloaded on 2/7/2026 3:14:08 PM. This article is licensed under a Creative Commons Attribution-NonCommercial 3.0 Unported Licence.

Synthesis of compound 3. To a solution of compound **1** (9 g, 45 mmol) and compound **2** (7.56 g, 40 mmol) in methanol (50 mL), $CuSO_4 \cdot 5H_2O$ (0.5 g, 2 mmol) in deionized water (0.2 mL) was added. After stirring for 30 min under nitrogen, the newly prepared sodium ascorbate solution (Vc: 0.66 g; $NaHCO_3$: 0.33 g) was added and stirred for 24 h at room temperature. $Na_2S \cdot 9H_2O$ (0.48 g, 2 mmol) was added, and after filtration, the filtrate was concentrated, diluted with dichloromethane, and dried over anhydrous $MgSO_4$. After removal of the solvent, the crude product was purified *via* column chromatography (ethyl acetate: methanol = 10 : 1) to yield compound **3** as a pale-yellow oil (8.3 g, yield 70.9%).

Synthesis of compound 4. Compound **3** (5 g, 13 mmol), CH_3I (2.49 mL, 40 mmol) and dichloromethane (5 mL) were added to a 50 mL reaction flask and stirred for 48 h at 45 °C until no compound **3** was detected *via* thin layer chromatography (TLC). The mixture was concentrated and dried under vacuum to generate compound **4** as a brown liquid (5 g, yield 73.5%).

Synthesis of T1. Compounds **4** (5 g, 10 mmol), methanol (10 mL), LiTFSI (5.7 g, 20 mmol) and deionized water (8 mL) were added to a 100 mL reaction flask and stirred at 70 °C for 3 days. The mixture was extracted with dichloromethane and washed with deionized water until the absence of AgI precipitation in the aqueous phase after the addition of $AgNO_3$ solution. The solution was concentrated and dried under vacuum to obtain **T1** as a brown oil (5.1 g, yield 86.9%).

Synthesis of compound 6. To a solution of compound **5** (4.7 g, 25 mmol) and compound **2** (5.7 g, 30 mmol) in methanol (80 mL), $CuSO_4 \cdot 5H_2O$ (0.313 g, 1.25 mmol) in deionized water (0.2 mL) was added. After stirring for 30 min under nitrogen, the newly prepared sodium ascorbate solution (Vc: 0.4 g; $NaHCO_3$: 0.2 g) was added and stirred for 24 h at room temperature. $Na_2S \cdot 9H_2O$ (0.3 g, 0.125 mmol) was added, and after filtration, the filtrate was concentrated, diluted with dichloromethane, and dried over anhydrous $MgSO_4$. After removal of the solvent, the crude product was purified *via* column chromatography (dichloromethane: methanol = 1 : 1) to yield compound **6** as a light-yellow oil (10 g, yield 71.4%).

Synthesis of compound 7. Compound **6** (6.4 g, 17 mmol), CH_3I (3.2 mL, 50 mmol) and methyl dichloride (10 mL) were added to a 50 mL reaction flask and stirred for 48 h at 45 °C until no compound **6** was detected *via* TLC. The mixture was concentrated and dried under vacuum to generate compound **7** as a brown oil (8.1 g, yield 92.1%).

Synthesis of T2. Compounds **7** (8 g, 15 mmol), methanol (20 mL), LiTFSI (9 g, 30 mmol) and deionized water (15 mL) were added to a 100 mL flask stirred at 70 °C for 3 days. The mixture was extracted with dichloromethane and washed with deionized water until the absence of AgI precipitation in the aqueous phase with the addition of $AgNO_3$ solution. The solution was concentrated and dried under vacuum to obtain **T2** as a brown oil (6 g, yield 74.1%).

Synthesis of compound 9. To a solution of compound **8** (4.38 g, 25 mmol) and compound **5** (5.64 g, 30 mmol) in methanol (80 mL), $CuSO_4 \cdot 5H_2O$ (0.313 g, 1.25 mmol) in deionized water (0.2 mL) was added. After stirring for 30 min under nitrogen, the newly prepared sodium ascorbate solution (Vc: 0.4 g; $NaHCO_3$: 0.2 g) was added and stirred for 24 h at room temperature. $Na_2S \cdot 9H_2O$ (0.3 g, 1.25 mmol) was added, and after filtration, the filtrate was concentrated, diluted with dichloromethane, and dried over anhydrous $MgSO_4$. After removal of the solvent, the crude product was purified using column chromatography (dichloromethane: methanol = 1 : 1) to yield compound **6** as a light-yellow oil (7 g, 77.1%).

Synthesis of compound 10. Compound **9** (2.68 g, 8 mmol), CH_3I (2.84 mL, 20 mmol) and methyl dichloride (10 mL) were added to a 50 mL reaction flask and stirred for 48 h at 45 °C until no compound **10** was detected *via* TLC. The mixture was concentrated and dried under vacuum to generate compound **10** as a brown liquid (3.5 g, yield 87.5%).

Synthesis of T3. Compound **10** (3 g, 6 mmol), methanol (10 mL), LiTFSI (3.4 g, 12 mmol) and deionized water (8 mL) were added to a 100 mL reaction flask and stirred at 70 °C for 3 days. The mixture was extracted with dichloromethane and washed with deionized water until the absence of AgI precipitation in the aqueous phase with the addition of $AgNO_3$ solution. The solution was concentrated and dried under vacuum to obtain **T3** as a brown oil (3 g, yield 89.6%).

Results and discussion

Synthesis and characterization of ILs

As shown in Scheme 1, triazoles **3**, **6**, and **9** with and without –OH groups were synthesized *via* Cu(I)-catalysed click chemistry using organic azides and alkynes, followed by alkylated and anion metathesis reaction, generating the target triazoliums ILs **T1**, **T2** and **T3**, and their NMR spectra can be seen in Fig. S1–S12.† The peaks in their ^{1}H NMR spectra at 7.77 ppm (Fig. S3†), 7.85 ppm (Fig. S7†) and 7.91 ppm (Fig. S10†) demonstrate the formation of triazole groups, respectively. After the

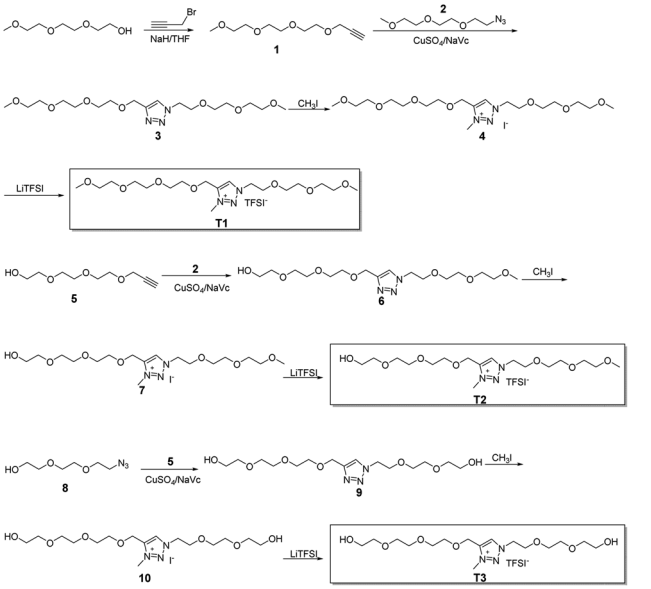

Scheme 1 Synthesis of triazolium ILs **T1**, **T2** and **T3**.

© 2022 The Author(s). Published by the Royal Society of Chemistry

Open Access Article. Published on 16 March 2022. Downloaded on 2/7/2026 3:14:08 PM.
This article is licensed under a Creative Commons Attribution-NonCommercial 3.0 Unported Licence.

quaternization of the triazole groups with CH_3I, the corresponding peaks shifted to 9.02 ppm (Fig. S4†), 9.03 ppm (Fig. S8†) and 9.18 ppm (Fig. S11†), respectively. Besides, the new peaks at 4.35 ppm (Fig. S4†), 4.38 ppm (Fig. S8†) and 4.40 ppm (Fig. S11†) are ascribed to the methyl protons attached to the N atom on the triazolium ring, as depicted in Scheme 1, which is in agreement with the literatures.[34,35] Furthermore, the peak area ratio of the triazolium protons to the methyl protons connected to the triazolium ring is 3 : 1. Thus, all the above-mentioned results confirm the successful quaternization. Usually, ILs with the $TFSI^-$ anion possess higher electrochemical stability and weaker interaction intensity with cations, which is beneficial for electrochemical applications.[36] Subsequently, the I^- anion was exchanged with the $TFSI^-$ anion, and the chemical shift of the triazolium protons shifted high-field relative to the corresponding triazolium iodide ILs (Fig. S5, S9 and S12,† respectively), showing that the anion exchange reactions proceeded completely. Additionally, the ^{13}C NMR spectra of the ILs (123–115 ppm, Fig. S5, S9 and S12,† respectively) indicate the successful introduction of the $TFSI^-$ anion.

Thermal properties

The thermal stability of ILs determines whether they be applied in high-temperature batteries, and thus the decomposition temperatures of the ILs were measured *via* thermogravimetric analysis (TGA). As shown in Fig. 1(a), **T1** without –OH groups displayed the highest thermal decomposition temperature (T_d, 5% weight loss) of 301 °C, whereas **T2** and **T3** displayed a lower T_ds than that of **T1**, indicating that the presence of –OH groups lowered the thermal stability of the ILs. This because –OH groups possess stronger polarity than that of $–OCH_3$, and hence display a lower activation energy for degradation during heating.[37,38] Furthermore, a low glass transition temperature (T_g) is beneficial for the rapid transportation of ions to some extent, especially in polyelectrolytes, and hence the T_gs of the ILs was measured *via* differential scanning calorimetry (DSC). Fig. 1(b) shows the DSC curves of **T1**, **T2** and **T3**. Similarly, **T1** displayed the lowest T_g of −59 °C, which is still was higher than that of imidazolium-based ILs with alkyl chains.[39] The presence of –OH and $–OCH_2–$ groups results in increased polarity and viscosity in ILs, which is not conducive to the movement of the segments in ILs, leading to a higher T_g.[40]

Ionic conductivity

The intrinsic conductivity of the ILs at different temperatures was investigated *via* electrochemical impedance spectroscopy (EIS) and the results are presented in Table 1, Fig. S13 and S14,† where **T1** presented the highest σ value at each temperature. For instance, at 30 °C, the conductivity of **T1** (0.88×10^{-3} S cm^{-1}) is about 3-times higher than that of **T3** (0.28×10^{-3} S cm^{-1}) and 1.5-times higher than that of **T2** (0.57×10^{-3} S cm^{-1}). The conductivity decreased with an increase in the number of terminal –OH groups also because the polarity of the –OH group is not conducive to ion transport. The above-mentioned DSC results also demonstrated this trend, that is, **T1** without –OH groups displayed the lowest T_g, and hence beneficial for ion migration and enhancement in conductivity.[41] Furthermore, an increase in temperature also improved the conductivity,[22] where the highest σ value of **T1** was 2.65×10^{-3} S cm^{-1} at 110 °C.

The above-mentioned results illustrate that **T1** possesses the best performance among the ILs, but its conductivity still need to be improved. An increase in ionic conductivity depends on efficient ion transport, including the number of ions, which is determined by the portion of salts added. Another factor is the mobility of ions, which depends on the ability of the molecules to move. More importantly, researchers have proposed the use of high concentration zinc salt and lithium salt electrolyte (usually 1 M Zn^{2+} and 20 M Li^+) to overcome the shortcomings of conventional aqueous ZIBs,[42] such as low Coulomb efficiency, hydrogen/oxygen evolution reaction, and dendrite growth

Table 1 Physicochemical properties of T1, T2 and T3

	$\sigma^a/\times10^{-3}$ S cm^{-1}						
ILs	30 °C	60 °C	90 °C	110 °C	T_g ^{b}/°C	$T_{d5\%}$ ^{c}/°C	ESW ^{d}/V
T1	0.88	1.71	2.37	2.65	−59	301	4.76
T2	0.57	1.46	2.23	2.55	−53	286	4.11
T3	0.28	1.14	1.98	2.39	−52	286	3.52

^{a} Determined by EIS. ^{b} Determined by DSC. ^{c} Determined by TGA. ^{d} Determined by LSV.

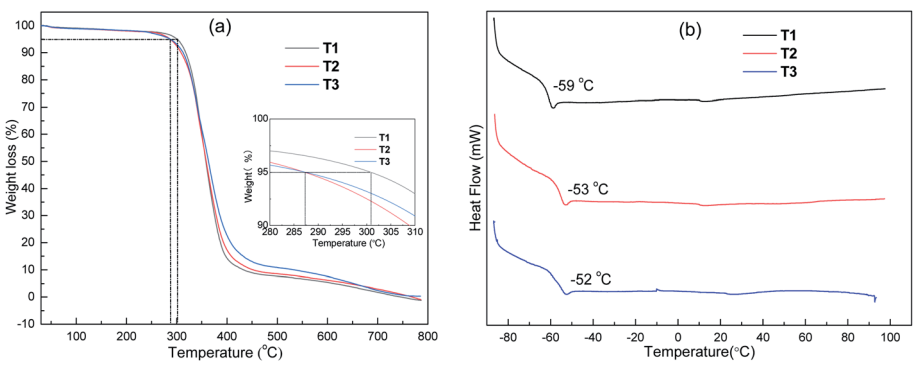

Fig. 1 (a) TGA and (b) DSC curves of T1, T2 and T3.

Open Access Article. Published on 16 March 2022. Downloaded on 2/7/2026 3:14:08 PM. This article is licensed under a Creative Commons Attribution-NonCommercial 3.0 Unported Licence.

during charge/discharge procedure. Herein, the IL-based electrolytes with 1 M $Zn(CF_3SO_3)_2$ and different amounts of LiTFSI were prepared by using **T1** as the solvent, which were denoted as **T1S-*x*** ($x = n_{Li}$: n_{Zn} = 5, 10, 15, 20, 21, and 25). The conductivity of **T1S-*x*** was calculated based on the measured Nyquist diagram, as shown in Fig. S15.† The conductivity increased with an increase in the amount of LiTFSI when x is less than 20 due to the increase in carrier LiTFSI salt. The maximum conductivity of 1.55×10^{-3} S cm^{-1} was realized when x was 20. Upon the further addition of LiTFSI, the conductivity decreased due to the increase in viscosity.[43] In comparison, an aqueous electrolyte with the concentration of 1 M $Zn(CF_3SO_3)_2$ + 20 M LiTFSI was prepared, which was denoted as **WS-20**, and its conductivity was determined to be 2.74×10^{-3} S cm^{-1} (calculated using the Nyquist diagram, Fig. S16†), which is higher than that of **T1S-20**. The conductivity of the two types of electrolytes reached the magnitude of 10^{-3} S cm^{-1}, and thus they could be used in ZIBs.

Electrochemical properties

Linear sweep voltammetry (LSV) was applied to investigate the electrochemical stability of the ILs by sandwiching them between a freshly polished stainless sheet and zinc sheet, and the results are shown in Fig. 2(a) and Table 1. Among them, **T1** displayed the widest ESW (4.76 V) with a cathodic limiting voltage of −1.19 V and anodic limiting voltage of +3.57 V, which is higher than that of imidazolium-based ILs with the $TFSI^-$ anion.[36,44] Due to the relatively poor stability of the –OH group, **T2** and **T3** showed narrower ESWs of 4.11 and 3.52 V, respectively. A similar phenomenon was reported for PEO-based solid polyelectrolyte with and without terminal –OH groups.[45] As reported previously, the addition of salt can reduce the "free" solvent in the system and decrease the reactivity of the solvent, thus improving the electrochemical stability.[46–48] Herein, the addition of salts resulted in a broader ESW of 6.36 V for **T1S-20** and 4.46 V for **WS-20** (Fig. 2(b)).

To evaluate the application of the ILs in ZIBs, $Zn/Li_3V_2(PO_4)_3$ batteries were prepared using **T1S-20** and **WS-20** as the electrolyte. Firstly, the cyclic voltammetry (CV) curves were tested for three cycles at a scanning rate of 0.1 mV S^{-1} at 30 °C. It can be seen in Fig. 3(a) that the **T1S-20** system showed two pairs of redox peaks at 1.39/1.47 V and 1.32/1.41 V, which are ascribed to the stepwise Li^+ extraction/insertion from/into the $Li_3V_2(PO_4)_3$ structure, respectively,[30,49] which exhibit a good degree of coincidence. In contrast, the **WS-20** system displayed a relatively large peak potential deviation (Fig. 3(b)), which may be due to polarization.[50]

Charge/discharge performance

Fig. 4(a) shows the rate performance of **T1S-*x*** and **WS-20** in the $Zn/Li_3V_2(PO_4)_3$ batteries at current densities of 0.2, 0.3, 0.5, 1.0 and 1.5 A g^{-1}. With an increase in the content of LITFSI added, the **T1S-*x*** system showed an improved initial capacity, and the battery with **T1S-20** delivered the highest initial capacity of 80 mA h g^{-1}, which is better than that of aqueous electrolyte-based $Zn/Li_3V_2(PO_4)_3$ batteries.[30] In comparison, the initial capacity of the **WS-20** system was 76 mA h g^{-1}, and the discharge capacity of the **T1S-20** system was higher than that of **WS-20** system at each rate. After adjusting the current density back to 0.2 A g^{-1}, the capacity of the **T1S-20** and **WS-20** systems was 79 and 67 mA h g^{-1}, respectively. With an increase in temperature to 80 °C, the capacities of both systems increased, where the **WS-20** system displayed a relatively large capacity attenuation after 30 cycles (Fig. 4(b)), while the **T1S-20** system could almost recover its initial capacity (111 mA h g^{-1}). Hence, the **T1S-20** system displayed a better rate performance in ZIBs.

Fig. 5 and 6 show the cyclic performance and Coulomb efficiency of the $Zn/Li_3V_2(PO_4)_3$ batteries based on the **T1S-20** and **WS-20** electrolytes at 30 °C and 80 °C. As shown in Fig. 5(a), the initial discharge capacity of the **T1S-20** and **WS-20** systems was 81 and 78 mA h g^{-1} at 30 °C, and after 50 cycles, the capacity retention rate of the **T1S-20** system was 89%, which is higher than that of the **WS-20** system (75%). Their initial discharge capacity and capacity retention rate are superior to that of imidazolium-IL-based Zn/polymer batteries, but much lower than that of the Zn/cobalt ferricyanide battery,[51–53] and hence the cathode materials also play a crucial role in the battery performance, as also concluded from our previous investigation.[30] In addition, the relatively low conductivity of the electrolytes was the main reason for the poor battery performances. At 80 °C, the initial discharge capacity of the two systems increased to 111 mA h g^{-1}, which is comparable to that of a ZIB with a $Zn(OTf)_2$-containing solid polymer electrolyte[54] and higher than that of the Zn/MnO_2 battery at high temperature.[55]

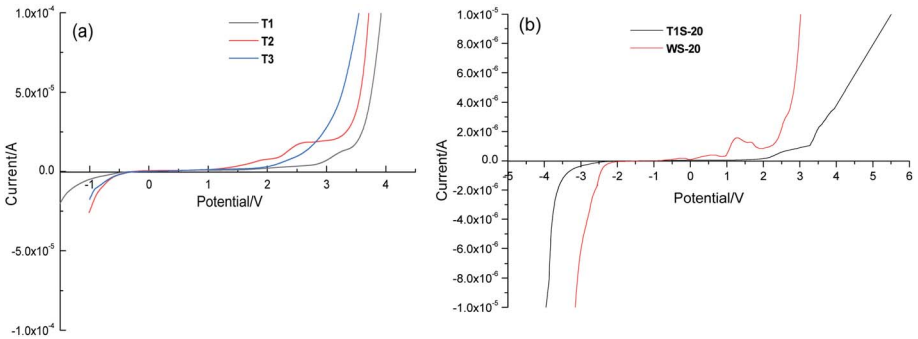

Fig. 2 Linear sweep voltammetry curves of (a) T1, T2, T3 and (b) T1S-20 and WS-20 at 30 °C.

© 2022 The Author(s). Published by the Royal Society of Chemistry

Open Access Article. Published on 16 March 2022. Downloaded on 2/7/2026 3:14:08 PM.
This article is licensed under a Creative Commons Attribution-NonCommercial 3.0 Unported Licence.

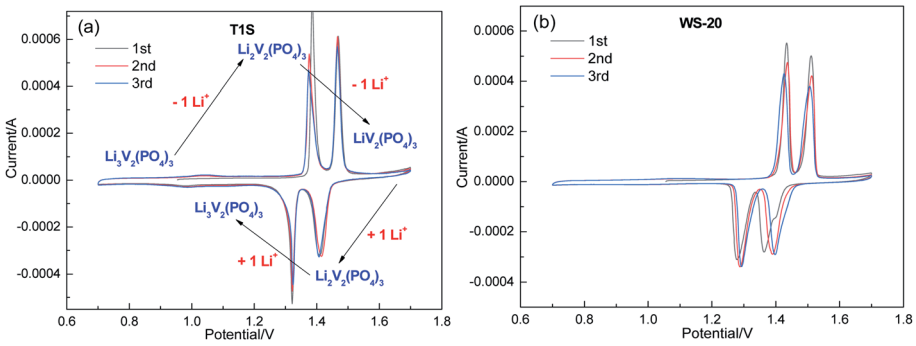

Fig. 3 CV curves of Zn/$Li_3V_2(PO_4)_3$ batteries with (a) **T1S-20** and (b) **WS-20** electrolyte at a scanning rate of 0.1 mV s^{-1}.

After 50 cycles, their discharge capacities decreased to 108 mA h g^{-1} (for **T1S-20**) and 100 mA h g^{-1} (for **WS-20**), together with the capacity retention rate of 98.2% and 90.9% (Fig. 5(b)), respectively. After 100 cycles, the capacity of the **WS-20** system was 79 mA h g^{-1} with a capacity retention rate of 71.8%, which is much lower than that of the **T1S-20** system (103.9 mA h g^{-1}, 93.6%). Hence, the **T1S-20** system has better cyclic stability than the **WS-20** system. As mentioned above, the electrode materials affect the performances of ZIBs, where dissolution of the cathode materials will reduce the utilization of the active substances[56] and side reactions will decrease the cycle stability and irreversibility. In the **WS-20** system, the presence of water would cause the dissolution of the cathode material and the formation of $(Zn(H_2O)_6)^{2+}$,[57] as well as dendrites. On the contrary, in the **T1S-20** system, its wide ESW, high thermal stability and absence of water guaranteed the stability of the battery.[48,58] Also, no molecules decomposed during the charge/discharge procedure to interact with vanadium and cause its dissolution.[56] Furthermore, no $(Zn(H_2O)_6)^{2+}$ was formed in the **T1S-20** system, which may generate a irreversibility issue in the Zn anode, and hence the **T1S-20** system-based ZIB displayed a better performance. Besides, it can be seen from Fig. 6(a) and (b) that the ZIBs exhibited a good charge and discharge efficiency with a Coulomb efficiency of 99%. With an increase in the temperature to 80 °C, the Coulomb efficiency of the **T1S-20** system remained at 99% (Fig. 6(c)), but that of the **WS-20** system displayed a slight decrease (97%) (Fig. 6(d)).

The constant current charge/discharge tests of **T1S-20** in the Zn/$Li_3V_2(PO_4)_3$ battery were carried out in the voltage range of 0.7–1.7 V at a current density of 0.2 A g^{-1} at 30 °C and 80 °C, respectively. As shown in Fig. 7(a), two platforms located at about 1.39 and 1.48 V can be observed during the charging process. The first platform (1.39 V) is ascribed to the first Li^+ ion extraction from $Li_3V_2(PO_4)_3$, resulting in the oxidation of V^{3+} to V^{4+}. The second platform (1.48 V) corresponds to the extraction of a second Li^+ ion with the transformation of $Li_2V_2(PO_4)_3$ to $LiV_2(PO_4)_3$. The discharge platforms are located at about 1.43 and 1.33 V, respectively, corresponding to the insertion of two Li^+ ions in the $LiV_2(PO_4)_3$ lattice with the reduction of V^{4+} to V^{3+}.[30,49] At 80 °C, similar platforms could be observed (Fig. 7(b)).

Fig. 8 depicts the Zn foil anode in the ZIBs after 50 cycles with the **WS-20** and **T1S-20** electrolytes at 30 °C, verifying the superiority of the ILs. After the batteries functioned for 50 cycles, the zinc foil anode and separator were taken out and washed with anhydrous tetrahydrofuran carefully three times, and then ethanol and deionized water in succession. As shown in Fig. 8(a), the dark separator indicates the dissolution of the cathode material in **WS-20**, and the lumps in the SEM image (Fig. 8(c)) confirm this. By contrast, the separator in Fig. 8(b)

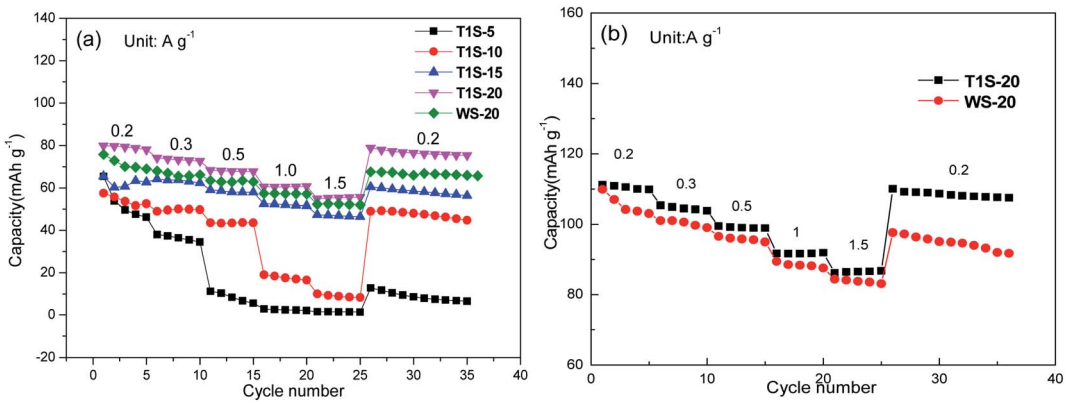

Fig. 4 Rate performance of Zn/$Li_3V_2(PO_4)_3$ battery with T1S-*x* and WS-20 electrolyte at different rates at (a) 30 °C and (b) 80 °C.

Open Access Article. Published on 16 March 2022. Downloaded on 2/7/2026 3:14:08 PM.
This article is licensed under a Creative Commons Attribution-NonCommercial 3.0 Unported Licence.

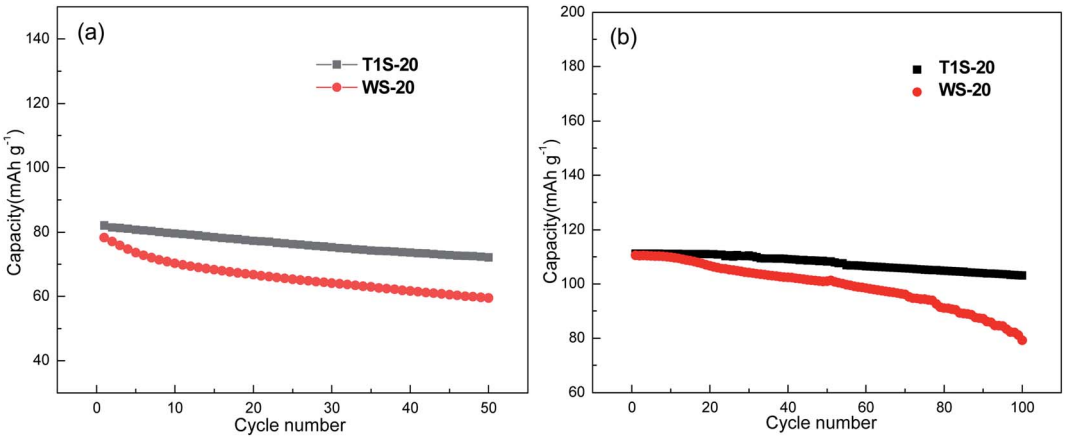

Fig. 5 Cyclic performance of Zn/$Li_3V_2(PO_4)_3$ batteries with **T1S-20** and **WS-20** electrolyte at (a) 30 °C and (b) 80 °C at a current density of 0.2 A g^{-1}.

was very clean, and no obvious dissolution of the cathode material was observed.

Subsequently, the high-temperature performance of the ZIBs was investigated. As shown in Fig. 9(a), after undergoing 100 cycles at 80 °C, the ZIB with the **WS-20** electrolyte became inflated, which restricts its application at high temperature, whereas the ZIB with the **T1S-20** electrolyte retained its initial shape (Fig. 9(b)). Similarly, the SEM images of their Zn foil anodes were measured. The Zn foil anode of the **WS-20** electrolyte-based ZIB displayed obvious dendrites and cathode dissolution (Fig. 9(c)), which is due to the accelerated water-induced side reaction, and a similar phenomenon was observed in aqueous ZIBs.[59] On the contrary, no obvious dendrites and cathode dissolution could be observed in the **T1S-20** electrolyte-based ZIB under the same condition (Fig. 9(d)). Therefore, the **T1S-20** electrolyte effectively alleviated the dissolution of the cathode material and displayed a good high-temperature performance.

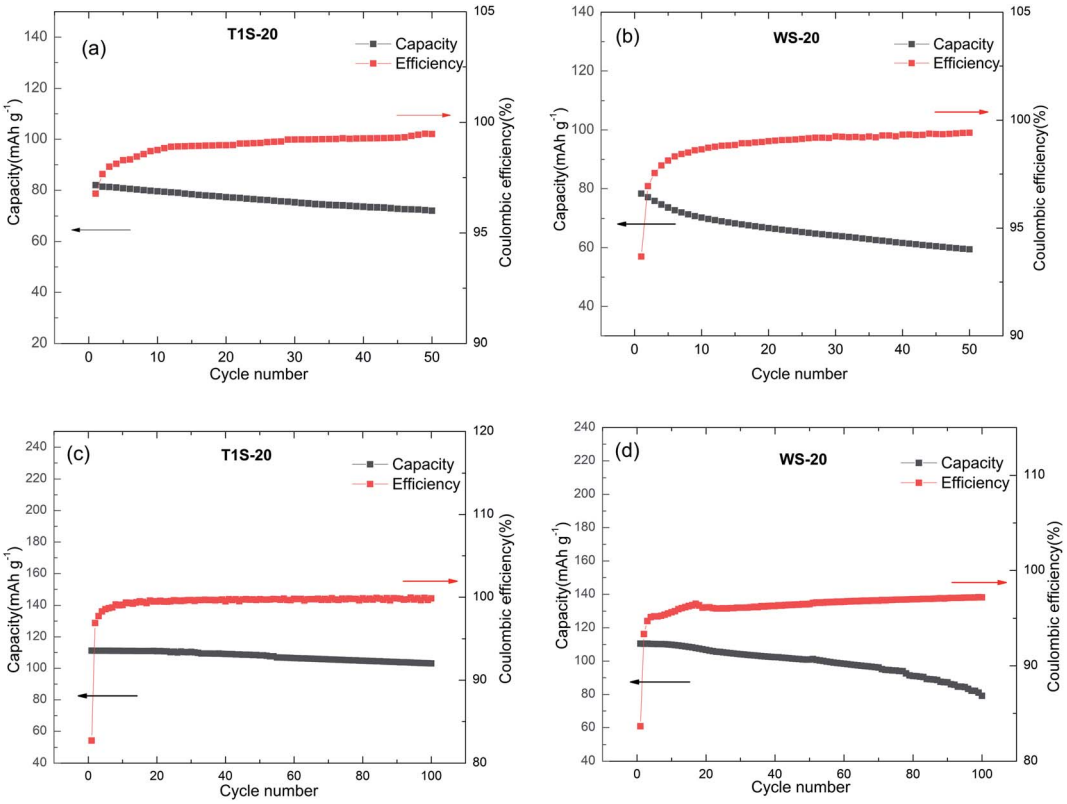

Fig. 6 Coulomb efficiency of Zn/$Li_3V_2(PO_4)_3$ batteries with different electrolytes at 0.2 A g^{-1}. (a) **T1S-20** at 30 °C, (b) **WS-20** at 30 °C, (c) **T1S-20** at 80 °C and (d) **WS-20** at 80 °C.

© 2022 The Author(s). Published by the Royal Society of Chemistry

Open Access Article. Published on 16 March 2022. Downloaded on 2/7/2026 3:14:08 PM.
This article is licensed under a Creative Commons Attribution-NonCommercial 3.0 Unported Licence.

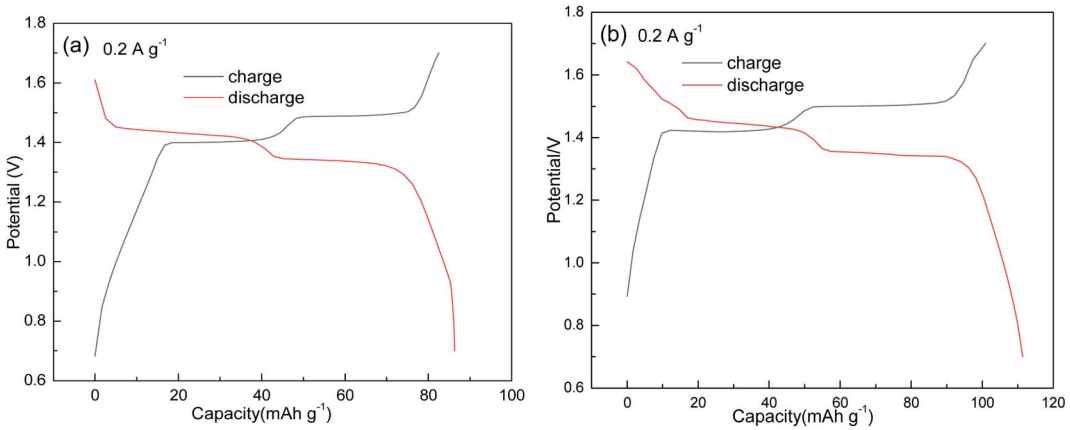

Fig. 7 First charge/discharge curves of Zn/$Li_3V_2(PO_4)_3$ batteries with **T1S-20** electrolyte at (a) 30 °C and (b) 80 °C.

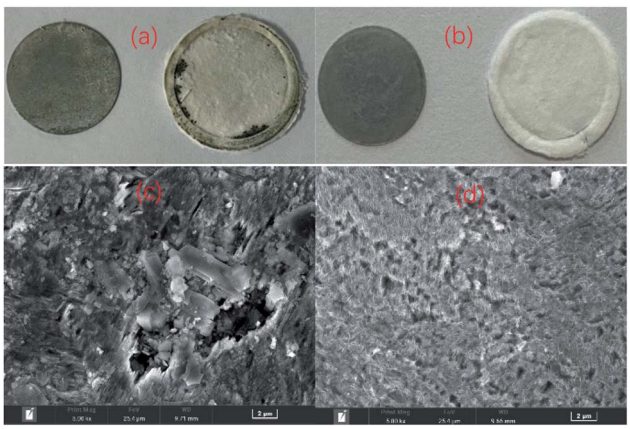

Fig. 8 Digital pictures and SEM images of Zn foil anode of Zn/$Li_3V_2(PO_4)_3$ batteries after 50 cycles with (a and c) **WS-20** and (b and d) **T1S-20** electrolyte at 30 °C, respectively.

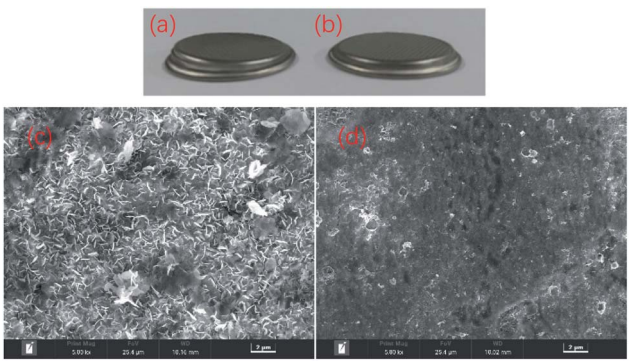

Fig. 9 Digital pictures and SEM images of Zn foil anode of Zn/$Li_3V_2(PO_4)_3$ batteries after 100 cycles with (a and c) **WS-20** and (b and d) **T1S-20** electrolyte at 80 °C.

Conclusions

Triazolium-based ILs **T1**, **T2** and **T3** with or without hydroxyl groups were prepared and **T1** without hydroxyl groups showed the best performance. By doping with $Zn(CF_3SO_3)_2$ and LiTFSI, the conductivity and ESW of **T1S-20** at 30 °C were 1.55 × 10^{-3} S cm^{-1} and 6.36 V, respectively. Based on this, Zn/$Li_3V_2(PO_4)_3$ ZIBs were assembled with **T1S-20** electrolyte and their cycle stability and rate performance were investigated at 30 °C and 80 °C. Simultaneously, aqueous ZIBs with the addition of the same salts (**WS-20**) were investigated for comparison. The **T1S-20**-based ZIB displayed a better performance, where after 50 cycles, its capacity retention rate was 89% at 30 °C, which was higher than that of the **WS-20**-based ZIB (75%). With an increase in the temperature to 80 °C, the superiority of the **T1S-20**-based ZIB was much more obvious, displaying a Coulomb efficiency of 99%. In addition, there were no obvious dendrites and cathode material dissolution in the **T1S-20**-based ZIB. Thus, all the results demonstrated that triazolium-based ILs can be used in high-temperature ZIBs, and triazolium-based ILs with different structures are currently under investigation to further improve their performance.

Conflicts of interest

There are no conflicts to declare.

Acknowledgements

The authors thank the National Natural Science Foundation of China (No. 21764006, 51862008, 52064014), Natural Science Foundation of Hunan Province, China (No. 2020JJ4505, 2017JJ3256), the Educational Commission of Hunan Province, China (No. 17B213, 202110531024), the Research Foundation of Jishou University of Hunan Province, China (No. Jdy20032) for the financial supports of this work.

Notes and references

1 C. Xu, B. Li, H. Du and F. Kang, *Angew. Chem., Int. Ed.*, 2012, **51**, 933–935.
2 Y. Zhao, Y. Zhu and X. Zhang, *InfoMat*, 2019, **2**, 237–260.

© 2022 The Author(s). Published by the Royal Society of Chemistry

Open Access Article. Published on 16 March 2022. Downloaded on 2/7/2026 3:14:08 PM. This article is licensed under a Creative Commons Attribution-NonCommercial 3.0 Unported Licence.

3 H. Pan, Y. Shao, P. Yan, Y. Cheng, K. S. Han, Z. Nie, C. Wang, J. Yang, X. Li, P. Bhattacharya, K. T. Mueller and J. Liu, *Nat. Energy*, 2016, **1**, 16039.
4 L. Suo, O. Borodin, T. Gao, M. Olguin, J. Ho, X. Fan, C. Luo, C. Wang and K. Xu, *Science*, 2015, **350**, 938–943.
5 J. Yan, J. Wang, H. Liu, Z. Bakenov, D. Gosselink and P. Chen, *J. Power Sources*, 2012, **216**, 222–226.
6 S. Bai, X. Li, Y. Wen, J. Cheng, G. Cao, Y. Yang and D. Li, *Acta Phys. Sin-Ch. Ed.*, 2016, **32**, 2007–2017.
7 S. Wu, Y. Wang, W. Liu, M. Ren, F. Kong, S. Wang, X. Wang, H. Zhao and J. Bao, *Inorg. Chem. Front.*, 2018, **5**, 3067–3073.
8 F. Tang, J. Gao, Q. Ruan, X. Wu, X. Wu, T. Zhang, Z. Liu, Y. Xiang, Z. He and X. Wu, *Electrochim. Acta*, 2020, **353**, 136570.
9 F. Tang, T. He, H. Zhang, X. Wu, Y. Li, F. Long, Y. Xiang, L. Zhu, J. Wu and X. Wu, *J. Electroanal. Chem.*, 2020, **873**, 114368.
10 X. Xie, S. Liang, J. Gao, S. Guo, J. Guo, C. Wang, G. Xu, X. Wu, G. Chen and J. Zhou, *Energy Environ. Sci.*, 2020, **13**, 503–510.
11 M. Song, H. Tan, D. Chao and H. J. Fan, *Adv. Funct. Mater.*, 2018, **28**, 1802564.
12 X. Song, H. He, M. Aboonasr Shiraz, H. Zhu, A. Khosrozadeh and J. Liu, *Chem. Commun.*, 2021, **57**, 1246–1249.
13 A. Wang, W. Zhou, A. Huang, M. Chen, Q. Tian and J. Chen, *J. Colloid Interface Sci.*, 2021, **586**, 362–370.
14 R. Feng, X. Chi, Q. Qiu, J. Wu, J. Huang, J. Liu and Y. Liu, *ACS Appl. Mater. Interfaces*, 2021, **13**, 40638–40647.
15 M. Becker, D. Rentsch, D. Reber, A. Aribia, C. Battaglia and R. S. Kuhnel, *Angew. Chem., Int. Ed.*, 2021, **60**, 14100–14108.
16 N. Zhang, F. Cheng, Y. Liu, Q. Zhao, K. Lei, C. Chen, X. Liu and J. Chen, *J. Am. Chem. Soc.*, 2016, **138**, 12894–12901.
17 N. Zhang, F. Cheng, J. Liu, L. Wang, X. Long, X. Liu, F. Li and J. Chen, *Nat. Commun.*, 2017, **8**, 405.
18 Y. Ye and Y. A. Elabd, *Macromolecules*, 2011, **44**, 8494–8503.
19 N. Chen, Y. Guan, J. Shen, C. Guo, W. Qu, Y. Li, F. Wu and R. Chen, *ACS Appl. Mater. Interfaces*, 2019, **11**, 12154–12160.
20 L. Liu, S. He, S. Zhang, M. Zhang, M. D. Guiver and N. Li, *ACS Appl. Mater. Interfaces*, 2016, **8**, 4651–4660.
21 Y. Jin, S. Fang, M. Chai, L. Yang and S. Hirano, *Ind. Eng. Chem. Res.*, 2012, **51**, 11011–11020.
22 J. Wu, J. Chen, J. Wang, X. Liao, M. Xie and R. Sun, *Polym. Chem.*, 2016, **7**, 633–642.
23 J. Wu, C. Wang, D. Zhou, X. Liao, M. Xie and R. Sun, *Macromol. Rapid Commun.*, 2016, **37**, 2017–2022.
24 D. Flachard, A. Serghei, M. Fumagalli and E. Drockenmuller, *Polym. Int.*, 2019, **68**, 1591–1598.
25 W. Deng, Z. Zhou, Y. Li, M. Zhang, X. Yuan, J. Hu, Z. Li, C. Li and R. Li, *ACS Nano*, 2020, **14**, 15776–15785.
26 J. Liu, N. Nie, J. Wang, M. Hu, J. Zhang, M. Li and Y. Huang, *Mater. Today Energy*, 2020, **16**, 100372.
27 X. Li, H. Wang, X. Sun, J. Li and Y. Liu, *ACS Appl. Energy Mater.*, 2021, **4**, 12718–12727.
28 K. Yoshii, T. Uto, N. Tachikawa and Y. Katayama, *Phys. Chem. Chem. Phys.*, 2020, **22**, 19480–19491.
29 S. Brutti, E. Simonetti, M. De Francesco, A. Sarra, A. Paolone, O. Palumbo, S. Fantini, R. Lin, A. Falgayrat, H. Choi, M. Kuenzel, S. Passerini and G. B. Appetecchi, *J. Power Sources*, 2020, **479**, 228791.
30 Y. Jiang, Q. Zou, S. Liu, H. Zeng, L. Chen, Y. Xiang, J. Li, X. Wu, J. Wu and L. Xiong, *J. Electroanal. Chem.*, 2021, **900**, 115685.
31 H. Li, C. Wang, X. Liao, M. Xie and R. Sun, *Polymer*, 2017, **112**, 297–305.
32 D. Basak, S. Christensen, S. K. Surampudi, C. Versek, D. T. Toscano, M. T. Tuominen, R. C. Hayward and D. Venkataraman, *Chem. Commun.*, 2011, **47**, 5566–5568.
33 H. Li, J. Wang, H. Han, J. Wu and M. Xie, *React. Funct. Polym.*, 2018, **127**, 20–28.
34 A. Jourdain, A. Serghei and E. Drockenmuller, *ACS Macro Lett.*, 2016, **5**, 1283–1286.
35 M. M. Obadia, A. Jourdain, P. Cassagnau, D. Montarnal and E. Drockenmuller, *Adv. Funct. Mater.*, 2017, **27**, 1703258.
36 Z. Liu, T. Cui, T. Lu, M. Shapouri Ghazvini and F. Endres, *J. Phys. Chem. C*, 2016, **120**, 20224–20231.
37 Z. Xue, Y. Zhang, X. Zhou, Y. Cao and T. Mu, *Thermochim. Acta*, 2014, **578**, 59–67.
38 J. Vuković, D. Steinmeier, M. D. Lechner, S. Jovanović and B. Božić, *Polym. Degrad. Stab.*, 2006, **91**, 1903–1908.
39 E. P. Yambou, B. Gorska and F. Béguin, *J. Mol. Liq.*, 2020, **298**, 111959.
40 C. Sirisopanaporn, A. Fernicola and B. Scrosati, *J. Power Sources*, 2009, **186**, 490–495.
41 M. Verma and H. Sahu, *Ionics*, 2015, **21**, 3223–3231.
42 F. Wang, O. Borodin, T. Gao, X. Fan, W. Sun, F. Han, A. Faraone, J. A. Dura, K. Xu and C. Wang, *Nat. Mater.*, 2018, **17**, 543–549.
43 X. Hu, R. Muchakayala, S. Song, J. Wang, J. Chen and M. Tan, *Int. J. Hydrogen Energy*, 2018, **43**, 3741–3749.
44 Z. Liu, T. Cui, G. Li and F. Endres, *Langmuir*, 2017, **33**, 9539–9547.
45 X. Yang, M. Jiang, X. Gao, D. Bao, Q. Sun, N. Holmes, H. Duan, S. Mukherjee, K. Adair, C. Zhao, J. Liang, W. Li, J. Li, Y. Liu, H. Huang, L. Zhang, S. Lu, Q. Lu, R. Li, C. V. Singh and X. Sun, *Energy Environ. Sci.*, 2020, **13**, 1318–1325.
46 M. Chen, J. Wu, T. Ye, J. Ye, C. Zhao, S. Bi, J. Yan, B. Mao and G. Feng, *Nat. Commun.*, 2020, **11**, 5809.
47 O. Borodin, *Curr. Opin. Electrochem.*, 2019, **13**, 86–93.
48 Z. Fang, Y. Luo, H. Liu, Z. Hong, H. Wu, F. Zhao, P. Liu, Q. Li, S. Fan, W. Duan and J. Wang, *Adv. Sci.*, 2021, **8**, 2100736.
49 C. Li, W. Yuan, C. Li, H. Wang, L. Wang, Y. Liu and N. Zhang, *Chem. Commun.*, 2021, **57**, 4319–4322.
50 D. Cheng, Y. F. Yang, J. L. Xie, C. J. Fang, G. Q. Zhang and J. Xiong, *J. Mater. Chem. A*, 2015, **3**, 14348–14357.
51 T. J. Simons, M. Salsamendi, P. C. Howlett, M. Forsyth, D. R. MacFarlane and C. Pozo-Gonzalo, *ChemElectroChem*, 2015, **2**, 2071–2078.
52 Z. Liu, A. Prowald, O. Höfft, G. Li, A. Lahiri and F. Endres, *ChemElectroChem*, 2018, **5**, 2321–2325.
53 L. Ma, S. Chen, N. Li, Z. Liu, Z. Tang, J. A. Zapien, S. Chen, J. Fan and C. Zhi, *Adv. Mater.*, 2020, **32**, 1908121.
54 Z. Chen, X. L. Li, D. H. Wang, Q. Yang, L. T. Ma, Z. D. Huang, G. J. Liang, A. Chen, Y. Guo, B. B. Dong, X. Y. Huang, C. Yang and C. Y. Zhi, *Energy Environ. Sci.*, 2021, **14**, 3492–3501.

© 2022 The Author(s). Published by the Royal Society of Chemistry

Open Access Article. Published on 16 March 2022. Downloaded on 2/7/2026 3:14:08 PM.
This article is licensed under a Creative Commons Attribution-NonCommercial 3.0 Unported Licence.

55 F. N. A. Mo, H. F. Li, Z. X. Pei, G. J. Liang, L. T. Ma, Q. Yang, D. H. Wang, Y. Huang and C. Y. Zhi, *Sci. Bull.*, 2018, **63**, 1077–1086.
56 H. N. Si, L. Li, W. J. Hao, L. Seidl, X. L. Cheng, H. Y. Xu, G. X. Jia, O. Schneider, S. L. An and X. P. Qiu, *ACS Appl. Energy. Mater.*, 2019, **2**, 5050–5056.
57 C. Liu, X. Xie, B. Lu, J. Zhou and S. Liang, *ACS Energy Lett.*, 2021, **6**, 1015–1033.
58 X. C. Wang, Z. F. Shang, A. K. Yang, Q. Zhang, F. Y. Cheng, D. Z. Jia and J. Chen, *Chem*, 2019, **5**, 364–375.
59 J. Huang, X. Chi, Y. Du, Q. Qiu and Y. Liu, *ACS Appl. Mater. Interfaces*, 2021, **13**, 4008–4016.